where $V_{load}$ is the voltage at load resistance, $R_{load}$ is the load resistance, and $Q_{in}$ is the solar power input in [W] on the surface of the $Al_2O_3$ absorber plate. Conversion efficiencies against heat flux for the 5 mm TOMs are presented in Figure 5c. The conversion efficiencies of the graphite-coated 5 mm TOM 1 and the SiC-coated 5 mm TOM 4 are higher than the efficiency of the uncoated 5 mm TOM 1 which is in agreement with the $P_{max}$ results. As for the 5 mm TOM 4, the fluctuation of $\eta$ (2nd point of the blue curve in Figure 5c) was caused by a combination of the radiation fluctuation (horizontal error bars) and the instability of $V_{load}$ (vertical error bars).

Figure 6a-d summarize the data of $P_{max}$ and $\eta$ *vs.* heat flux and *T5 – T6* for 4, 5 and 10 mm TOMs coated by graphite (5 mm TOM 4 coated by SiC). Depending on the temperature difference *T5 – T6* the maximum output power $P_{max}$ increases as $P_{max} \sim f(\Delta T^2)$ and a maximum value of 54.4 mW was achieved for a leg length of 10 mm at a heat flux of 9.5 W cm$^{-2}$ (5th point in Figure 6a). A maximum output power of 88.8 mW was obtained for the 5 mm TOM 4 at a heat flux of 14.4 W cm$^{-2}$ and a temperature difference of *T5 – T6* = 622 K. A conversion efficiency of 0.082% was obtained for a TOM with 10 mm leg length and an $Al_2O_3$ absorber area of 30 × 30 mm$^2$ (Figures 6b, d). As expected longer TE legs lead to higher conversion efficiency [24].

The conversion efficiency is higher at higher heat fluxes resulting in higher temperature differences *T5 – T6* which improves the Carnot efficiency. The conversion efficiency reaches the maximum for 4 mm TOMs around 4 W cm$^{-2}$, for 5 mm TOMs between 4–8 W cm$^{-2}$ and for 10 mm TOMs around 6 W cm$^{-2}$. After reaching the maximum value, the conversion efficiency decreases because of a degradation of the graphite at high temperatures when the heat flux exceeds 7.5 W cm$^{-2}$. A further reason for decrease of the conversion efficiency are the re-radiation losses from the $Al_2O_3$ absorber plate. The re-radiation losses from the $Al_2O_3$ absorber plate increase with $T^4$.

As the radiation losses are difficult to measure directly, a simulation procedure was developed [25]. The results show that there is no significant radiation between the $Al_2O_3$ absorber plates and the TE legs, but the major heat losses of ~ 60% are due to the re-radiation from the hot side of the $Al_2O_3$ absorber plate.

In an ideal case the internal resistance $R_{int}$ of the module is equal to the resistance of the thermoelectric oxide material $R_{mater}$. However, in real thermoelectric modules, the effect of the contact resistance on the conversion is not negligible. It is well known that high contact resistances lower the conversion efficiency of the devices remarkably. The internal resistances, contact resistances and resistances of the material for the TOMs were evaluated for the highest applied ΔT based on the following equations:

$$R_{\text{int}} = R_{mater} + R_{cont}, \text{ where } R_{mater} = 2\frac{l}{A}\int_{T6}^{T5}(<\rho_p> + <\rho_n>)(T_5 - T_6) \tag{3}$$

$$R_{\text{int}} = \frac{V_{OC}^2}{4P_{\max}} \text{ when } R_{load} = R_{\text{int}}. \tag{4}$$

**Figure 6.** Maximum output power and conversion efficiency of the TOMs as a function of the heat flux (a, b) and the temperature difference between the hot and the cold plate (c, d).

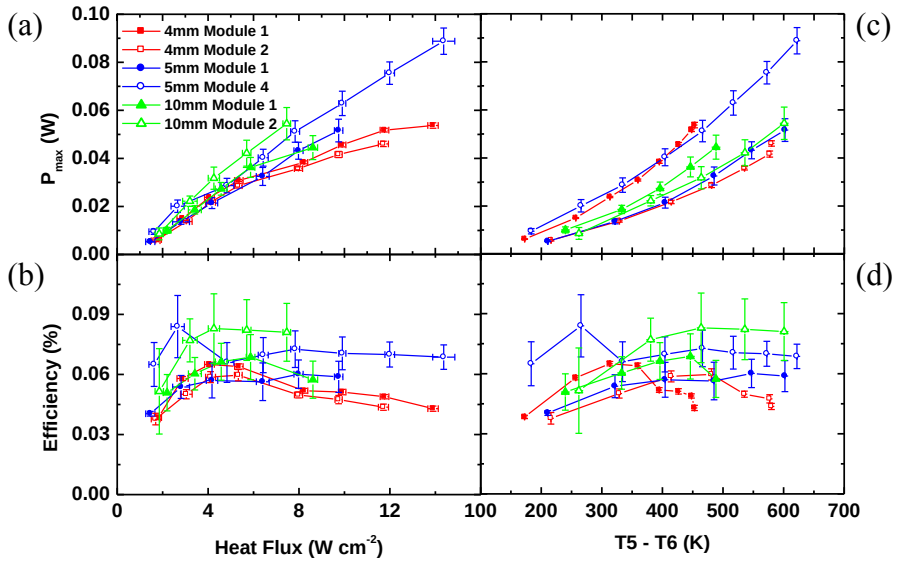


The results are summarized in Table 2 as well as the other relevant physical parameters, such as average values of Seebeck coefficient and electrical resistivity of *p*- and *n*-type TE legs for all TOMs. The internal resistance increases with leg length because of the increase of the $R_{mater}$. The contact resistance vary in the range of 0.29 Ω < $R_{cont}$ < 0.64 Ω depending on the manufacturing quality of TOMs.

**Table 2.** Physical parameters of four–leg TOMs.

| | ΔT [K] | A/l [mm] | $\langle S_p \rangle$ [μV K$^{-1}$] | $\langle S_n \rangle$ [μV K$^{-1}$] | $\langle \rho_p \rangle$ [mΩ cm] | $\langle \rho_n \rangle$ [mΩ cm] | $R_{int}$ [Ω] | $R_{mater}$ [Ω] | $R_{cont}$ [Ω] | MQF1 [%] | MQF2 [%] |
|---|---|---|---|---|---|---|---|---|---|---|---|
| 4 mm TOM 1 | 453 | 5.06 | 162.0 | -230.8 | 37.8 | 30.0 | 0.86 | 0.27 | 0.59 | 23 | 31 |
| 4 mm TOM 2 | 580 | 5.06 | 179.3 | -223.5 | 36.3 | 28.9 | 0.84 | 0.26 | 0.58 | 11 | 31 |
| 5 mm TOM 1 | 602 | 4.05 | 182.6 | -220.4 | 35.6 | 28.5 | 0.96 | 0.32 | 0.64 | 14 | 33 |
| 5 mm TOM 4 | 622 | 4.05 | 179.8 | -221.9 | 35.9 | 28.7 | 0.61 | 0.32 | 0.29 | 23 | 52 |
| 10 mm TOM 1 | 489 | 2.03 | 171.3 | -227.4 | 37.1 | 29.4 | 1.15 | 0.66 | 0.49 | 38 | 57 |
| 10 mm TOM 2 | 601 | 2.03 | 173.2 | -226.1 | 37.0 | 29.0 | 1.26 | 0.65 | 0.61 | 31 | 52 |

$\langle S_p \rangle$, $\langle S_n \rangle$, $\langle \rho_p \rangle$ and $\langle \rho_n \rangle$ is the average Seebeck coefficient for *p*-type, *n*-type leg and average electrical resistivity for *p*-type, *n*-type leg, respectively.

The more detailed determination of the contact resistance was done by measurement of 5 mm *n*-type TE leg at several temperature differences which vary from 0 K to 410 K. The measurement configuration is shown in Figure 7a. From the evaluation of $\langle \rho_n \rangle$ and the internal resistance $R_{int}$ measurement, the contact resistance on the hot side $R_{conthot}$ and the cold side $R_{contcold}$ of the 5 mm *n*-type leg was determined. The evaluation of $R_{conthot}$, $R_{contcold}$ and $R_{int}$ was done based on the following equations:

$$R_{\text{int}} = \int_{T_6}^{T_5} R_{mater} \frac{d(T_5 - T_6)}{T_5 - T_6} + R_{contcold} + R_{conthot} \tag{5}$$

$$R_{xy} = \int_{T_{6+Z}}^{T_5} R_{mater,Y} \frac{d(T_5 - T_{6+Z})}{T_5 - T_{6+Z}} + R_{conthot} \tag{6}$$

$$R_{yz} = \int_{T_{6+Y+Z}}^{T_5} R_{mater,X} \frac{d(T_5 - T_{6+Y+Z})}{T_5 - T_{6+Y+Z}} + R_{contcold} \tag{7}$$

The data of the contact resistance measurement were normalized and plotted in Figure 7b. It was shown, that the major contribution to internal resistance is the contact resistance on the cold side and the hot side of the TOM compared to the resistance of the thermoelectric oxide materials. Thus, it can be concluded that for better conversion experiments the contacts have to be improved to decrease the contact resistance of the TOMs by e.g. developing better contact materials.

**Figure 7.** Contact resistance measurement configuration based on Equations 5-7 (a) and normalized $R_{int}$, $R_{mater}$, $R_{contcold}$ and $R_{conthot}$ for 5 mm *n*-type TE leg (b).

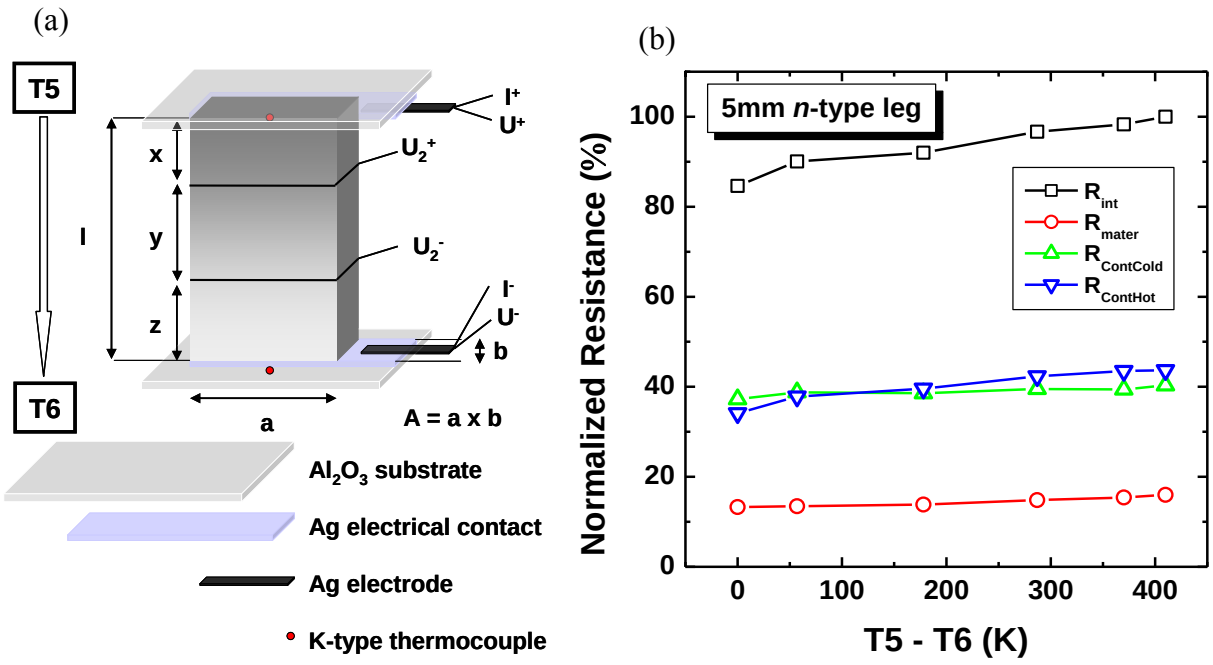


Quantitative measures of the device quality are the manufacture quality factors *MQF1*, and *MQF2* [24,26]. These factors were calculated to determine the eventual ambiguity associated with the manufacturing defects of TOMs based on the following equations:

$$MQF1 = \frac{P_{\max}}{N\Delta T^2 \left(S^2 / 2\rho\right)\left(A / l\right)}, \tag{8}$$

$$MQF2 = \frac{R_{mater}}{R_{\text{int}}} \tag{9}$$

where $N$ is the number of thermocouples in a TOM, $\Delta T$ is the temperature gradient between the hot side and the cold side of the TOM, $S$ is the Seebeck coefficient, $\rho$ is the electrical resistivity, $A$ is the cross-sectional area of TE leg and $l$ is the leg length. The manufacture quality factors vary in the range of 11% < *MQF1* < 38% and 31% < *MQF1* < 57%, respectively. The manufacture quality factor values calculated by using Equation 9 were comparable with previous studies on thermoelectric oxide modules [26]. In the case of the 5 mm TOM 1 with $P_{max}$ = 51.6 mW and 5 mm TOM 4 with $P_{max}$ = 88.8 mW it was evident that the maximum output power was enhanced by lowering the contact resistance. The manufactory quality factor measured under a similar temperature gradients of the 5 mm TOM 4 was *MQF2* = 52% while the 5 mm TOM 1 revealed a different MQF of *MQF2* = 33%.

## 4. Conclusions

Four-leg thermoelectric oxide modules, combining *p*- and *n*-type thermoelements made of $La_{1.98}Sr_{0.02}CuO_4$ and $CaMn_{0.98}Nb_{0.02}O_3$, respectively, were successfully used to directly convert simulated solar radiation into electrical energy by using a HFSS as energy source. The Figure of Merit ZT of the *p*- and *n*-type thermoelectric materials was evaluated up to 800 K showing nearly constant values at higher temperatures for the *p*-type and a linear increase with temperature up to ZT = 0.08 for the *n*-type material. The electrical resistivity of both materials shows metallic behavior with $\rho$ between 20 - 24 mΩ cm at and $|S| \geq 160$ μV $K^{-1}$ at T = 300 K. The temperature gradient along the TE legs was almost linear showing a lower value for the *p*-type legs compared to the *n*-type legs due to a higher thermal conductivity of the *p*-type material above T = 400 K.

It was shown that coatings of the hot $Al_2O_3$ absorber plate by graphite induced a larger temperature gradient in the TOMs and the maximum output power and the conversion efficiency were significantly improved. A heat flux between 4–8 W $cm^{-2}$ resulted in the highest conversion efficiency. The maximum conversion efficiency of 0.082% was obtained for a TOM with 10 mm leg length. With a slightly modified geometry of the TOM the conversion efficiency would be ~ 0.4% [25]. It was found that the contact resistances which vary in the range of 0.29 Ω < $R_{cont}$ < 0.64 Ω are limiting the conversion efficiency significantly. Thus, besides the necessity of the development of better thermoelectric materials and the lowering of re-radiation losses, a major part in the improvement of solar thermoelectric converters applied at high temperatures with concentrated solar radiation will be to reduce substantially the contact resistances.

## Acknowledgements

We acknowledge the Swiss Federal Office of Energy and Swiss National Foundation for financial support. We would also like to thank A. Hämmerli and P. Hinz for technical support and A. Shkabko for contact resistance discussions.

## References and Notes

1. Nayak, P.D.K. Two Days National Seminar on Alternative Energy Sources; In Proceedings of V.P.M.'s Polytechnic: Thane, India, 2005.

2. Steinfeld, A. Solar thermochemical production of hydrogen–a review. *Sol. Energy* **2005**, *78*, 603-615.
3. Steinfeld, A.; Palumbo, R. Solar Thermochemical Process Technology. In *Encyclopedia of Physical Science & Technology*; Meyers, A., Ed.; Academic Press: San Diego, CA, USA, 2001; Volume 15, pp. 237-256.
4. Tritt, T.M.; Böttner, H.; Chen, L. Thermoelectrics: Direct solar thermal energy conversion. *Mater. Res. Bull.* **2008**, *33*, 366-368.
5. Yang, J.; Caillat, T. Thermoelectric materials for space and automotive power generation. *Mater. Res. Bull.* **2006**, *31*, 224-229.
6. Kim, S.S.; Yin, F.; Kagawa, Y. Thermoelectricity for crystallographic anisotropy controlled Bi-Te based alloys and p-n modules. *J. Alloys Compd.* **2006**, *419*, 306-311
7. Yamashita, O.; Sugihara, S. High-performance bismuth-telluride compounds with highly stable thermoelectric figure of merit. *J. Mater. Sci.* **2005**, *40*, 6439-6444.
8. Reddy, E.S.; Noudem, J.G.; Hebert, S.; Goupil, C. Fabrication and properties of four-leg oxide thermoelectric modules. *J. Phys. D: Appl. Phys.* **2005**, *38*, 3751-3755.
9. Shin, W.; Muruyama, N.; Ikeda, K.; Sago, S. Thermoelectric power generation using Li-doped NiO and (Ba, Sr)$PbO_3$ module. *J. Power Sources* **2001**, *103*, 80-85.
10. Funahashi, R.; Mikami, M.; Mihara, T.; Urata, S.; Ando, N. A portable thermoelectric-power-generating module composed of oxide devices. *J. Appl. Phys.* **2006**, *99*, 066117.
11. Funahashi, R.; Matsubara, I.; Ikuta, H.; Takeuchi, T.; Mizutani, U.; Sodeoka, S. Oxide single crystal with high thermoelectric performance in air. *Japan. J. Appl. Phys.* **2000**, *39*, 1127-1129.
12. Funahashi, R.; Urata, S.; Mizuno, K.; Kouuchi, T.; Mikami, K. $Ca_{2.7}Bi_{0.3}Co_4O_9$/$La_{0.9}Bi_{0.1}NiO_3$ thermoelectric devices with high output power density. *Appl. Phys. Lett.* **2004**, *85*, 1036-1038.
13. Terasaki, I.; Sasago, Y.; Uchinokura, K. Large thermoelectric power in $NaCo_2O_4$ single crystal. *Phys. Rev. B* **1997**, *56*, 12685-12687.
14. Ito, M.; Nagira, T.; Furumoto, D.; Katsuyama, S.; Nagai, H. Synthesis of $Na_xCo_2O_4$ thermoelectric oxides by the polymerized complex method. *Scr. Mater*. **2003**, *48*, 403-408.
15. Zhou, S.; Zhao, J.; Chu, S.; Shi, L. Synthesis, characterization and magnetic properties of lightly doped $La_{2-x}Sr_xCuO_4$ (x = 0.04) nanoparticles. *Phys. C* **2007**, *451*, 38-43.
16. Bocher, L.; Robert, R.; Aguirre, M.H.; Malo, S.; Hébert, S.; Maignan, A.; Weidenkaff, A. Thermoelectric and magnetic properties of perovskite-type manganate phases synthesised by ultrasonic spray combustion (USC). *Solid State Sci.* **2008**, *10*, 496-501.
17. Weidenkaff, A. Preparation and application of nanostructured perovskite phases. *Adv. Eng. Mater*. **2004**, *6*, 709-714.
18. Aguirre, M.H.; Canulescu, S.; Robert, R.; Homazava, N.; Logvinovich, D.; Bocher, L.; Lippert, T.; Döbeli, M.; Weidenkaff, A. Structure, microstructure, and high-temperature transport properties of $La_{1-x}Ca_xMnO_{3-\delta}$ thin films and polycrystalline bulk materials. *J. Appl. Phys.* **2008**, *103*, 013703.
19. Tomeš, P.; Robert, R.; Trottmann, M.; Bocher, L.; Aguirre, M.H.; Hejtmánek, J.; Weidenkaff, A. Synthesis and characterization of new ceramic thermoelectrics implemented in a thermoelectric oxide module. *J. Electron. Mater.* **2010**, doi:10.1007/s11664-010-1214-4.

20. Hirsch, D.; Zedtwitz, P.V.; Osinga, T.; Kinamore, J.; Steinfeld, A. A new 75 kW high-flux solar simulator for high-temperature thermal and thermochemical research. *J. Sol. Energy Eng.* **2003**, *125*, 117-120.
21. Bocher, L.; Aguirre, M.H.; Logvinovich, D.; Shkabko, A.; Robert, R.; Trottmann, M.; Weidenkaff, A. $CaMn_{1-x}Nb_xO_3$ ($x \leq 0.08$) perovskite-type phases as promising new high-temperature n-type thermoelectric materials. *Inorg. Chem*. **2008**, *47*, 8077-8085.
22. Snyder, G.J. Application of the compatibility factor to the design of segmented and cascaded thermoelectric generators. *Appl. Phys. Lett.* **2004**, *84*, 2436-2438.
23. Bramson, M.A. *Infrared Radiation—A Handbook of Applications*; Plenum Press: New York, NY, USA, 1968.
24. Rowe, D.M.; Min, G. Evaluation of thermoelectric modules for power generation. *J. Power Sources* **1998**, *73*, 193-198.
25. Suter, C.; Tomeš, P.; Steinfeld, A.; Weidenkaff, A. Heat transfer and geometrical analysis of thermoelectric converters driven by concentrated solar radiation. *Materials* **2010**, *3*, 2735-2752.
26. Lemonnier, S; Goupil, Ch.; Noudem, J.; Guilmeau, E. Four-leg $Ca_{0.95}Sm_{0.05}MnO_3$ unileg thermoelectric device. *J. Appl. Phys.* **2008**, *104*, 014505.